International Journal of Fatigue 161 (2022) 106917

Contents lists available at ScienceDirect

International Journal of Fatigue

journal homepage: www.elsevier.com/locate/ijfatigue

A crystal plasticity approach to understand fatigue response with respect to pores in additive manufactured aluminium alloys

Mengzhen Cao, Yang Liu *, Fionn P.E. Dunne

Department of Materials, Imperial College London, London SW7 2AZ, United Kingdom

ARTICLE INFO

Keywords:
Fatigue crack nucleation
Pore
Fatigue life prediction
Crystal Plasticity
Additive manufacturing

ABSTRACT

A crystal plasticity finite element modelling method integrated with a stored energy density criterion is utilized to comparatively investigate fatigue crack nucleation behaviour and quantify fatigue life with respect to different pore types in AlSi10Mg fabricated by selective laser melting. Representative microstructural models show that fatigue crack nucleation exhibits high sensitivity to both gas/keyhole and lack of fusion pores, but particularly the latter, which leads to much lower fatigue life at high stress levels. Multi-intragranular slip system activations occurring at the sharp corners of lack of fusion pores contribute to substantial increase in local geometrically necessary dislocation density. Together with the rapid accumulation of slip, these drive high local stored energy density at the tips of lack of fusion pores. For gas/keyhole pores, high stresses lead to pore-induced shear band formation which shifts the origin of crack nucleation away from the pore to other microstructural features. At low stresses, fatigue life for lack of fusion and gas/keyhole pores tend to converge but remain shorter than for pore-free microstructures.

1. Introduction

The increasing demand for engineering components with higher complexity in both shape and functionality has made additive manufacturing (AM) an appealing technique for processing metallic materials due to its high flexibility for fabrication. Ideally, parts with any complex geometries could be fabricated by AM and the number of parts in a single assembly could be reduced by merging multiple components into one entity, which permits engineers higher freedom in design [1]. Selective laser melting (SLM) is one such state-of-the-art AM technique to process metallic components that require high performance and precision. SLM uses powders as the feedstock, which are supplied to the building chamber in layers and melted by the laser according to the designated path followed by rapid solidification of the liquid metal [2]. The same process is carried out repeatedly until numerous layers of solidified metal are deposited to form the final part.

However, AM has yet to achieve success for safety–critical components because of the existence of numerous manufacturing defects which may develop, of which pores are the most frequently observed [3,4] and classified into three types: entrapped gas, keyholing and lack of fusion (LOF) pores [2]. Entrapped gas pores are typically small and spherical in shape, and form because of either shielding gas trapped within the material during solidification, or pre-existing gas in powder feedstock or material vaporization [5]. Keyhole pores form when the laser beam energy is high and penetrates multiple layers resulting in deep melt pools, and if not carefully controlled, the latter collapse and leave voids near the bottom of melt pools [6]. Keyhole pores are normally near-spherical and frequently found in regions with unusually high energy density input such as laser turning points [7]. Lack of fusion occurs when there is insufficient energy input, leaving un-melted area between layers or scan tracks and the flowability of molten metal is too low to fill this gap since the energy input is not sufficient [8]. As a result, LOF defects are generally larger than keyholing and entrapped gas pores, with irregular shape, high aspect ratio, and longitudinal axis perpendicular to the building direction.

AlSi10Mg is a bespoke aluminium alloy for AM with good castability and low shrinkage as a result of the Al-Si eutectic, as well as good mechanical properties that make it applicable to a wide range of applications [8,9]. The chemical composition of AlSi10Mg is listed in Table 1. However, due to the low laser absorptivity, high thermal conductivity and highly oxidative nature of Al [3,10], controlling defect formation resulting from SLM processing of AlSi10Mg remains challenging.

The existence of pores is a potential threat to the mechanical properties of AM components, especially fatigue performance [5]. And pores

* Corresponding author.
E-mail address: yang.liu@imperial.ac.uk (Y. Liu).

https://doi.org/10.1016/j.ijfatigue.2022.106917
Received 9 November 2021; Received in revised form 23 March 2022; Accepted 9 April 2022
Available online 12 April 2022

Table 1
Typical chemical composition of AlSi10Mg powder used for SLM [9].

Element	Al	Si	Mg	Mn	Fe	Cu
Mass fraction (wt. %)	Balance	9.0–11.0	0.45–0.60	≤0.45	≤0.55	≤0.1

are difficult to be effectively eliminated, such that AM parts are known to suffer from poor structural integrity. Fatigue crack nucleation constitutes a significant part of the fatigue life for many engineering alloys [11]. In general, the large sizes and irregular morphologies of LOF pores give rise to higher stress concentration at sharp corners, driving plastic deformation under cyclic loading and thus contributing to earlier nucleation of fatigue cracks [5,8,12]. Experimental studies confirm that most fatigue cracks starting from pores in SLM samples initiate from LOF [13–16], manifesting an extremely high sensitivity of fatigue crack nucleation to LOF. But fatigue cracks initiating from other pore types are rarely reported. Apart from size and shape, the location of the pores is another important factor and fatigue cracks are more prone to initiate from surface defects than internal defects [1,14,17]. These multiple factors can result in more damaging circumstances when LOF occurs near or in contact with an outer surface [18].

Fatigue crack nucleation with respect to pores in SLM components is therefore of great significance for improving their structural integrity and there remains considerable need for mechanistic understanding. Phenomenological, semi-empirical and fracture mechanics models have been investigated for fatigue life prediction of AM materials incorporating the effective defect size into the models [19]. Beretta et al. [20] summarized AM alloys fatigue data suggesting scatter is significantly reduced when the fatigue strength is correlated with the critical defect size. Romano et al. [21] utilized a modified stress intensity factor ΔK to predict fatigue life based on a plasticity corrected NASGRO-type equation, capturing the slope of experimental S-N curves for SLM AlSi10Mg, presuming homogeneous microstructures and semi-circular surface defects.

These approaches treat the material as continuum and do not reflect the role of microstructure nor local mechanistic drivers of nucleation [11,22]. Heterogeneity of microstructure may not be the only factor in fatigue behaviour of AM alloys, but its role is worthy of investigation because of the interactions between pores and the local surrounding microstructures which are unique to AM processing methods.

Recent microstructurally-sensitive crystal plasticity finite element (CPFE) modelling approaches have attempted to capture fatigue crack nucleation [11,22–24] addressing key quantities local to observed crack nucleation sites including stress, plastic strain, dislocation density and plastic energy [11,23,25]. Wan et al. [26] proposed a stored energy density criterion in which the underpinning mechanistic explanation for nucleation was argued to be new surface generation by energy release from (predominantly) relaxation of lattice curvature supported by geometrically necessary dislocations (GND). Chen et al. [27,28] successfully captured slip-driven fatigue crack nucleation cites using this criterion in multiple single crystal, oligocrystal and polycrystal Ni-based superalloy samples. Stored energy density has also shown effectiveness for microstructure-sensitive short fatigue crack growth [29].

Prithivirajan and Sangid [30,31] studied the role of pore size and pore cluster on fatigue crack nucleation in SLM IN718, also using a CPFE approach, investigating plastic strain accumulation, elastic anisotropy and triaxiality local to the pores. They observed a critical pore size comparable to grain size was needed to initiate fatigue failure, else the fatigue crack nucleation was found to be more sensitive to microstructural heterogeneities. In addition to pores, Zhang et al. [32] also introduced inclusions into their CPFE simulation of fatigue in SLM AlSi10Mg and concluded that pores give rise to more plastic strain accumulation in its vicinity than that of an inclusion. These studies idealized all pores into circles or spheres, which is observed for keyholing and entrapped gas pores in AM [5,7]. However, it is necessary to distinguish the pore types with respect to their shapes since fatigue crack nucleation in AM parts exhibits a very high sensitivity to LOF. Yeratapally et al. [12] idealized keyholing and entrapped gas pores as spherical while shaping LOF into a super ellipsoid in their CPFE modelling of fatigue response in IN718 [12]. The strain accumulation at the tip of LOF pore was found to be 37.8% higher than for a spherical pore, indicating higher susceptibility of fatigue crack nucleation to LOF. However, very limited insights were provided into the underlying mechanistic driver for the high sensitivity, and the interactions between pores and local microstructures are still not fully understood.

The stored energy density has been demonstrated to be a microstructure-sensitive mechanistic driver that enables determination not only of the site of crack nucleation, but also the cycles required to drive it [26,28,33,34]. It therefore potentially offers mechanistic insight into the propensity for the differing AM pore types to cause fatigue failure, and facilitates a ranking of the damage which results as a function of pore type, size and shape, with respect to characterised microstructural features. In addition, once the critical stored energy density has been determined, it becomes possible to establish S-N curves for representative AM microstructures containing the differing pore types.

This study comparatively investigates the micromechanical influence of differing pore types on the fatigue crack nucleation behaviour in SLM AlSi10Mg at various cyclic stress levels, aiming to provide more in-depth mechanistic explanations from the stored energy density point of view for the high fatigue sensitivity of pores that have been much experimentally observed in AM materials. Meanwhile, the interactions between pores and surrounding microstructures on driving fatigue cracks and their relation to applied stress levels are examined to reflect the microstructure-sensitive nature of fatigue crack nucleation. In what follows, Section 2 presents the modelling framework established for quantitative evaluation of micromechanical fatigue responses for a typical SLM AlSi10Mg microstructure containing differing pore types. Section 3 addresses the fatigue crack nucleation and lifetime predictions for the pore types under different stress levels, and the most damaging type of pore is identified, together with discussion of the results. Finally, Section 4 is for conclusions.

2. Methods

2.1. Crystal plasticity finite element modelling

A crystal plasticity finite element (CPFE) modelling framework is used to investigate the micromechanical responses of SLM AlSi10Mg, based on a code originally developed by Dunne et al. [35]. The crystal plasticity model is implemented in a user material subroutine utilizing ABAQUS standard/explicit analysis. Key equations are outlined for the CPFE framework in the following.

The total deformation gradient $\mathbf{F}$ is multiplicatively divided into elastic $\mathbf{F}^e$ (which contains lattice stretch and rigid body rotation) and plastic $\mathbf{F}^p$ (which contributes to dislocation slip) parts:

$$\mathbf{F} = \mathbf{F}^e\mathbf{F}^p \tag{1}$$

where $\mathbf{F}^e$ is determined from Hooke's law for anisotropic elasticity, and $\mathbf{F}^p$ is determined from plastic velocity gradient $\mathbf{L}^p$, which contains plastic deformation rate tensor $\mathbf{D}^p$ and plastic spin rate tensor $\mathbf{W}^p$. $\mathbf{L}^p$ results from the contribution of all slip systems activated:

$$\mathbf{L}^p = \mathbf{D}^p + \mathbf{W}^p = \dot{\mathbf{F}}^p\mathbf{F}^{p^{-1}} = \sum_{\alpha=1}^{12} \dot{\gamma}^\alpha \mathbf{s}^\alpha \otimes \mathbf{n}^\alpha \tag{2}$$

where $\mathbf{s}^\alpha$ and $\mathbf{n}^\alpha$ are the line vectors of slip direction and slip plane normal of the α^{th} slip system, respectively. Al is an FCC metal and there are 12 individual slip systems in FCC structure. Dislocation slip is activated in a given slip system once its resolved shear stress (RSS) τ^α exceeds the critical resolved shear stress (CRSS) τ_c^α.

Once the slip system α is activated, its slip rate $\dot{\gamma}^{\alpha}$ is expressed by the slip rule:

$$\dot{\gamma}^{\alpha} = \rho_m b^2 \nu \exp\left(-\frac{\Delta H}{kT}\right) \sinh\left(\frac{\Delta V}{kT}|\tau^{\alpha} - \tau_c^{\alpha}|\right) \tag{3}$$

in which ρ_m is the mobile dislocation density, ν the jump frequency of dislocations attempting to overcome energy barriers to glide, b Burgers vector magnitude, and ΔH the activation energy for pinned dislocation escape, with the associated activation volume ΔV. k is the Boltzman constant and T the operating temperature. The slip system strength τ_c^{α} evolves according to the Taylor hardening rule:

$$\tau_c^{\alpha} = \tau_{c0} + G_{12} b \sqrt{\rho_{GND} + \rho_{SSD}} \tag{4}$$

where τ_{c0} is the intrinsic critical resolved shear stress, G_{12} is the shear modulus, while ρ_{GND} and ρ_{SSD} represent the density of geometrically necessary (GND) and statically stored (SSD) dislocations. Thus, τ_c^{α} is not constant but evolves with sessile SSD and GND densities. The density of SSD is simply governed by the accumulation of plastic strain p, given by:

$$\dot{\rho}_{SSD} = \lambda \dot{p} \tag{5}$$

$$\dot{p} = \left(\frac{2}{3}\mathbf{D}^p : \mathbf{D}^p\right)^{\frac{1}{2}} \tag{6}$$

$$p = \int \dot{p} dt \tag{7}$$

where λ is the hardening coefficient determining the rate of SSD accumulation.

GNDs arise as a result of strain gradient which accommodate lattice curvature, and the components of GND are computed from the Nye dislocation tensor **Λ**, given by.

$$\mathbf{\Lambda} = \mathrm{curl}(\mathbf{F}^p) = \sum_{\alpha=1}^{12} \rho_{Gs}^{\alpha} \mathbf{b}^{\alpha} \otimes \mathbf{m}^{\alpha} + \rho_{Get}^{\alpha} \mathbf{b}^{\alpha} \otimes \mathbf{t}^{\alpha} + \rho_{Gen}^{\alpha} \mathbf{b}^{\alpha} \otimes \mathbf{n}^{\alpha} \tag{8}$$

in which ρ_{Gs}^{α} represents the density of screw component, and ρ_{Get}^{α} and ρ_{Gen}^{α} the edge components on slip system α. $\mathbf{b}^{\alpha}$ is the Burgers vector, $\mathbf{m}^{\alpha}$, $\mathbf{t}^{\alpha}$ and $\mathbf{n}^{\alpha}$ are the three unit vectors composing an orthogonal system. The L_2-norm minimization method is adopted in determining the final GND density, expressed as the sum of the squares of the three components for all slip systems:

$$\rho_{GND} = \sqrt{\sum_{\alpha=1}^{12} \left[(\rho_{Gs}^{\alpha})^2 + (\rho_{Get}^{\alpha})^2 + (\rho_{Gen}^{\alpha})^2\right]} \tag{9}$$

A stored energy density criterion has been proposed [26] and argued to be a primary mechanistic driver for fatigue crack nucleation [26–28]. The major part of the energy generated during plastic deformation is dissipated thermally or acoustically, whereas the rest is considered to be stored in dislocation structures. As a result, the stored energy is intrinsically associated with the length scale introduced by the mean free distance of dislocation structures. The dislocation structures are established and evolve with progressing cyclic loading, hence the local stored energy density also accumulates until at given site, it is high enough to generate new free surfaces, i.e. nucleation of fatigue crack. This critical value of G is the critical stored energy density G_c.

The total energy per cycle per unit volume generated by plastic deformation may be calculated over a complete saturated cycle from:

$$\dot{U} = \int |\boldsymbol{\sigma} : \mathbf{D}^p| dt \tag{10}$$

The volume within which the energy is stored by the establishment of dislocation structures is referred to as the storage volume ΔV_s, which is expressed in terms of the mean free distance λ' of sessile SSDs and GNDs, in addition to the potential free surface area ΔA_s:

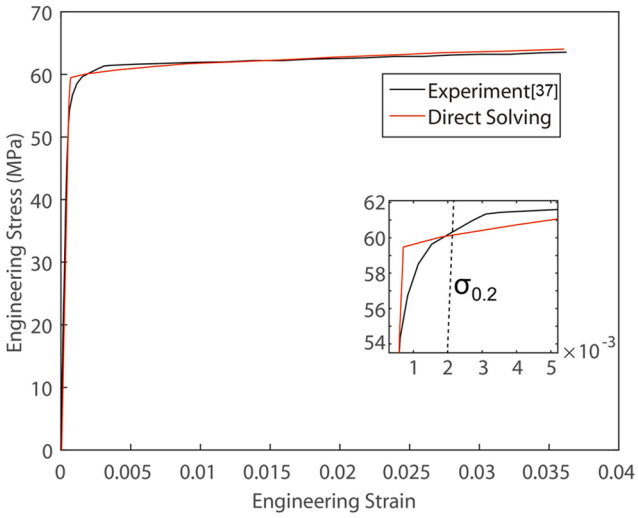

Fig. 1. Experimental stress–strain response of Al single crystal tension along [1 1 1] crystallographic orientation [37] in comparison with calibration results through direct solving of constitutive equations, with inset showing a magnification of the transition period.

$$\Delta V_s = \lambda' \Delta A_s = \frac{\Delta A_s}{\sqrt{\rho_{SSD} + \rho_{GND}}} \tag{11}$$

The fraction of plastic energy stored in dislocation structures is denoted ξ which is argued to stabilize through the formation of dislocation structures, and is taken as 0.05 [26,27,36]. This enables the calculation of cyclic stored energy density rate $\dot{G}$ as:

$$\dot{G} = \frac{\dot{U}\Delta V_s}{\Delta A_s} = \int \frac{\xi |\boldsymbol{\sigma} : \mathbf{D}^p| dt}{\sqrt{\rho_{SSD} + \rho_{GND}}} \tag{12}$$

The stored energy density G is consequently computed from the integration of $\dot{G}$ over loading cycles:

$$G = \int \dot{G} dN \tag{13}$$

The CPFE model enables the full-field distributions of stress, plastic strain and dislocation densities to be determined, such that the distribution of stored energy density may also be obtained to investigate the fatigue crack nucleation site in SLM AlSi10Mg. Once a critical value G_c is determined, the quantification of fatigue life to crack nucleation becomes feasible, which is described in detail in Section 3.3.

2.2. Material properties calibration

In order to acquire the material slip properties used in the CPFE modelling described above, an experimental macroscopic tensile stress–strain curve for pure Al single crystal is firstly utilised [37], in which the loading direction is [1 1 1] with respect to the crystal coordinate system. A direct solving of constitutive equations at an integration point is performed to simulate and compare with the single crystal tensile response. The model is subjected to the same loading conditions as in the experiment. The single crystal properties including the intrinsic critical resolved shear stress τ_{c0}, hardening coefficient λ, and elastic constants are acquired to best match the independent experimental data.

The magnitude of Burgers vector b (0.286 nm) is taken from [38]. The activation volume ΔV controls the strain rate sensitivity (SRS) [35] and it is set to be high enough ($400b^3$) to eliminate rate-dependent effects [39]. The dislocation jump frequency ν is set to be 1×10^{11} s^{-1} [23] and activation energy ΔH is determined to be 0.75 eV [40]. The calibration results are shown in Fig. 1, in which the simulated uniaxial stress–strain response of the Al single crystal is in good agreement with

Table 2
Al single crystal properties obtained after calibration.

C_{11} (GPa)	C_{12} (GPa)	C_{44} (GPa)	τ_{c0} (MPa)	b (μm)	λ (μm^{-2})	ΔV(μm^3)	ΔH(J/atom)	ν (s^{-1})
125.4	70.3	31	12.3	2.86×10^{-4}	0.3	$400b^3$	1.2×10^{-19}	1×10^{11}

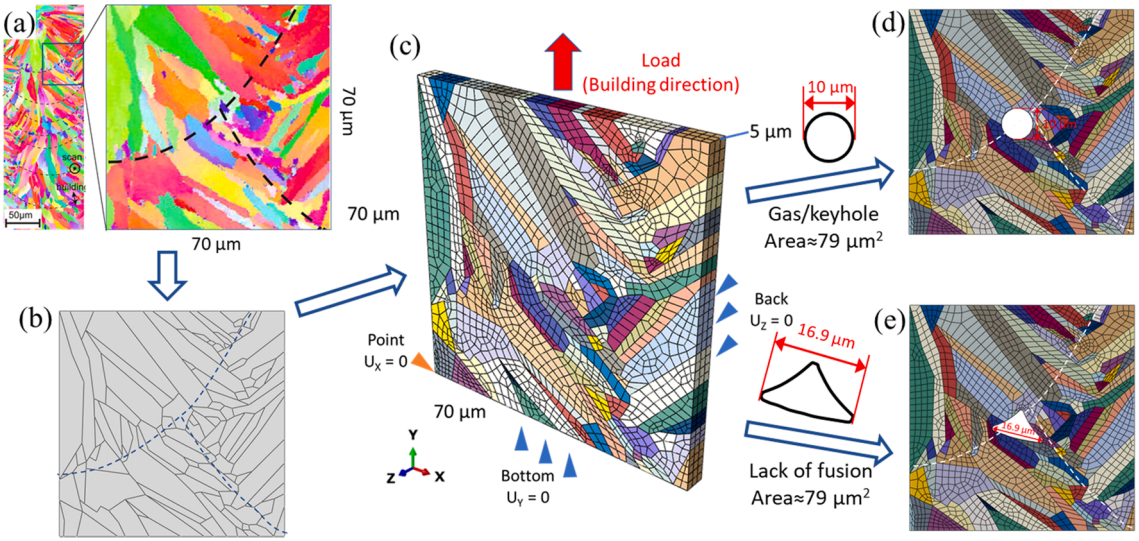

Fig. 2. The framework for microstructure construction: (a) an experimental EBSD IPF map from which the square microstructure for the CPFE model is taken, the dashed lines represent the melt pool boundaries [41], (b) the 2D microstructure sketch, (c) the 3D microstructure model with applied boundary conditions, (d-e) microstructures with gas/keyhole pore and LOF pore inserted, respectively.

experiment, showing very close yield strength $\sigma_{0.2}$ and hardening rate. The extracted single crystal properties of Al are listed in Table 2.

Note that these calibrated properties are for pure Al, instead of the alloy of interest AlSi10Mg which is a two-phase alloy and contains cellular Si substructures that contribute considerably to the strength of this alloy [41,42]. Hence the strengthening effect of the Si phases must be considered in order to properly describe the mechanical behaviour of AlSi10Mg, which is discussed in Section 2.4.

2.3. Microstructure reconstruction

Fig. 2(a) presents an electron backscattered diffraction (EBSD) inverse pole figure (IPF) map showing the side view of the microstructure of SLM AlSi10Mg processed using a bidirectional scanning strategy with no rotation between layers [41], in which the grain morphologies and melt pool structures can be identified. The model microstructure used for CPFE modelling is constructed based on this IPF map. A 70 μm × 70 μm square region at a melt pool 'triple junction' is selected for analysis, convenient for inserting potential pores later, since LOF tends to form between layers or melt pools [3], and keyholing tends to appear near the bottom of melt pools [6].

The 2D pore-free microstructure, as demonstrated in Fig. 2(b), is constructed by manually sketching the grain boundaries in ABAQUS CAE according to what is shown in the square region. Since the EBSD IPF map does not provide sub-surface information, the 2D microstructure is then extruded along the Z-direction with a thickness of 5 μm, similar to experimentally measured average grain size, to make it a 3D model. Guan et al. [43] have shown that this quasi-2D crystal plasticity approach can capture surface strains measured by digital image correlation (DIC) for single and oligo-crystals. For polycrystals, like SLM AlSi10Mg, this approach may not be able to reproduce experimental absolute results, whereas Chen et al. [28] have shown the quasi-2D approach enables a quantitative comparison of the key metrics with respect to fatigue crack nucleation for fixed, given microstructural representation of polycrystalline Ni alloys, which therefore serves the comparative purpose herein. The model is meshed with 2 μm global element size (5604 elements in total) using C3D20R element type. A convergence study of the meshing density is included in the Appendix. Due to the absence of exact information of crystallographic orientation of each grain, the microstructure is assigned with a random texture which is generated using MTEX toolbox [44] in MATLAB. The meshed 3D microstructure model is shown in Fig. 2(c).

To simplify the pore geometry while preserving the most important features, the entrapped gas pores and keyholing are idealized into circular pores just as in other studies [12,30,32] with 10 μm diameter, whereas the LOF is designed to be near-triangular with three arc sides to represent their irregular shapes and high aspect ratio observed in experiments [7,16]. In order to avoid too intense deformation occurring at the corners of the LOF defect, and to improve computational stability, the sharp corners of the LOF are smoothened to have a radius of 0.8 μm, and its size is chosen to an area same as that for gas/keyhole pore. This study therefore focuses on the shapes of the pores and their influence on local mechanical response of SLM AlSi10Mg. The two pores are both placed near the melt pool triple junction to accord with their formation preference. In particular, the meshing around the pores, especially at their corners, is refined to improve the convergence locally. The microstructure models embedded with gas/keyhole and LOF pores respectively are shown in Fig. 2(d) and (e).

The boundary and loading conditions selected are such that the Z-displacement normal to the back face is fixed to be zero ($U_Z = 0$), while the Y-displacement normal to the bottom face is also set to be zero ($U_Y = 0$). Uniaxial loading is applied uniformly on the top face along Y-direction, which is also the building direction during SLM. In addition, a single node point in the left bottom corner is fixed in the X-direction ($U_X = 0$) to prevent rigid body translation of the model. The remaining surfaces are free. The boundary conditions used for microstructures with pores are basically the same as above, except that some constraints in the back face ($U_Z = 0$) at the surrounding region of pores are removed to improve computational stability. As a result, the models are designed to comparatively show the influence of pore shape on the micromechanical

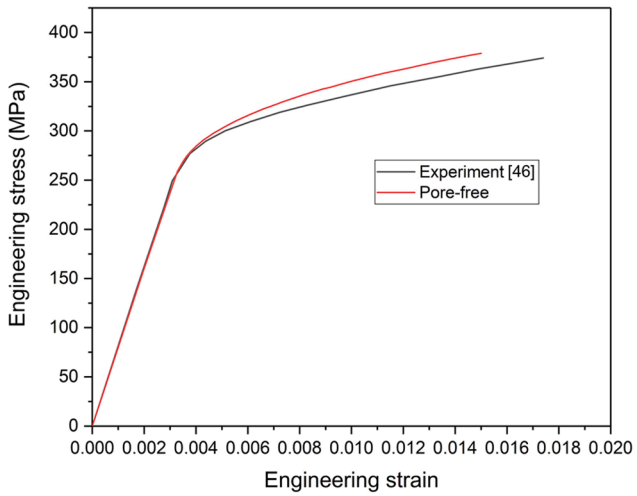

Fig. 3. The macroscopic tensile stress–strain curves obtained for the pore-free CPFE model in comparison with experiment [46].

behaviour of a small free-surface region within a side of a SLM AlSi10Mg sample built in the vertical orientation using a bidirectional scanning strategy with no scan rotation between layers, subjected to uniaxial loading.

2.4. Tensile and fatigue analysis

The strengthening effect of the very fine cellular substructures in SLM AlSi10Mg has not yet been reflected in the Al single crystal slip rule calibration, which is now addressed. Romanova et al. [45], addressed the modified slip system CRSS to include the strengthening of grain boundaries and cellular-dendritic substructures in SLM AlSi10Mg, given by:

$$\tau_c^{\alpha} = \tau_{c0} + k_1 D_i^{-1/2} + k_2 < d >^{-1/2} + f\left(\varepsilon_{eq}^{p}\right) \tag{14}$$

where the second term accounts for grain boundary strengthening, the third term represents the cell strengthening and the last term the strain hardening. In the CPFE slip rule used here, the grain boundary effect is incorporated through GND evolution, and the hardening from local plastic strain is included through SSD evolution as shown in Eqs. (5)–(7). Therefore, only the cell strengthening effect needs to be addressed in the equation for τ_c^{α}:

$$\tau_c^{\alpha} = \tau_{c0} + k_2 d^{-1/2} + G_{12} b \sqrt{\rho_{SSD} + \rho_{GND}} \tag{15}$$

in which k_2 is a fitting constant and is taken to be 0.7 MPa•cm$^{1/2}$ as reported in [45], while d is the average size of the cellular substructures and is set to be 0.5 μm in accordance with [45]. This average cell size is similar to experimental observations by Thijs et al. [41]. Thus, the resulting second term in Eq. (15) is calculated to be 99 MPa to include the cell strengthening from the Si phase in SLM AlSi10Mg. The pore-free model microstructure is subjected to monotonic loading up to 1.5% engineering strain. The resulting macroscopic stress–strain response is compared with experimental stress–strain data [46] in Fig. 3. While the fit between computed and experimental uniaxial stress–strain responses could be improved (by moderating the hardening coefficient), the independently determined parameters are preferred since a very good capture of the experimental elasticity and yield point has been achieved which is key for addressing fatigue with low levels of plasticity.

In order to investigate the fatigue behaviour of the three microstructures with differing pores, cyclic loading with different stress levels is applied. The cyclic loading conditions are chosen to include those used in the fatigue test presented in [47] in order to utilise the experimental fatigue life to determine the critical stored energy density G_c (see Section 3.3). The maximum cyclic stress σ_{max} is set to be between 0.4 and ~ 1.0 times the yield strength ($\sigma_{0.2NP}$) of the model polycrystal microstructure but with no pore present. The latter was determined to be 313 MPa after obtaining the polycrystal tensile stress–strain curve. In the cyclic loading, the applied stress ratio R is 0.1 with cyclic frequency 30 Hz, applied for 20 cycles at which point the analyses reach a steady cyclic state. Littlewood et al. [48] demonstrated that dislocation densities and slip accumulation evolve at near constant cyclic rates after the first few fatigue cycles. A schematic of the first two cyclic loading cycles is shown in Fig. 4(a), and (b) presents the overall cyclic stress–strain response for pore-free microstructure showing progressive strain accumulation. The computational time for each cyclic simulation varies from about 20 min for the simplest case (pore-free microstructure at the lowest stress level) to about one day for the worst scenario (LOF pore microstructure at the highest stress level).

3. Results and discussion

3.1. Fatigue behaviour at high stress levels

3.1.1. Sensitivity of fatigue crack nucleation to pores

The consequent fatigue responses for the three model microstructures (pore-free, gas/keyhole and LOF pores) are assessed in detail to investigate the detrimental effect of pores to fatigue performance of SLM AlSi10Mg, especially its fatigue crack nucleation behaviour. Applied peak stress σ_{max} below about $0.7\sigma_{0.2NP}$ leads to very limited plasticity for the pore-free microstructure, suggesting that this is the fatigue limit for this microstructure. Stresses in excess of σ_{max} $0.9\sigma_{0.2NP}$ for the LOF pore microstructure in particular lead to very short fatigue lives, hence determining the loading range of interest.

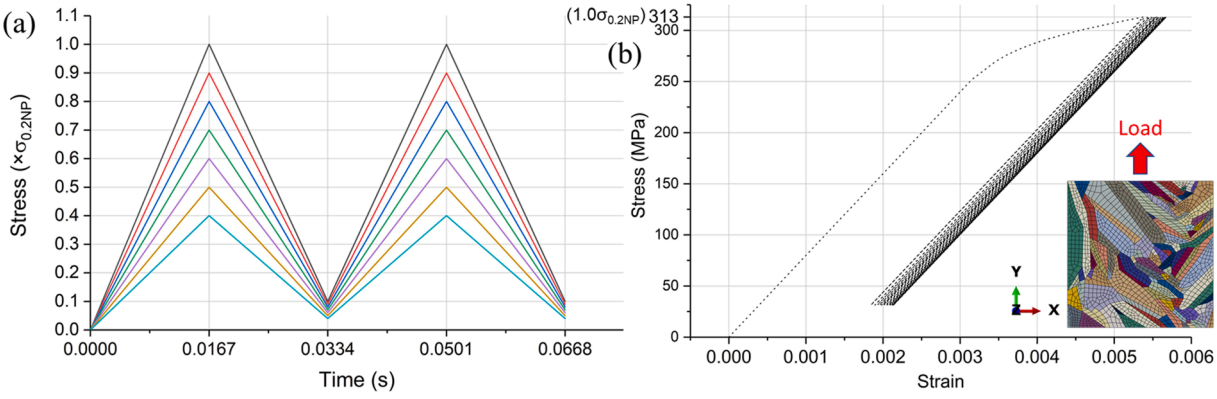

Fig. 4. (a) Applied cyclic loading conditions under σ_{max} between 0.4 and ~ 1.0 times $\sigma_{0.2NP}$ for the first two cycles, and (b) overall cyclic stress–strain response as $\sigma_{max} = 1.0\sigma_{0.2NP}$ for pore-free model microstructure shown in the inset.

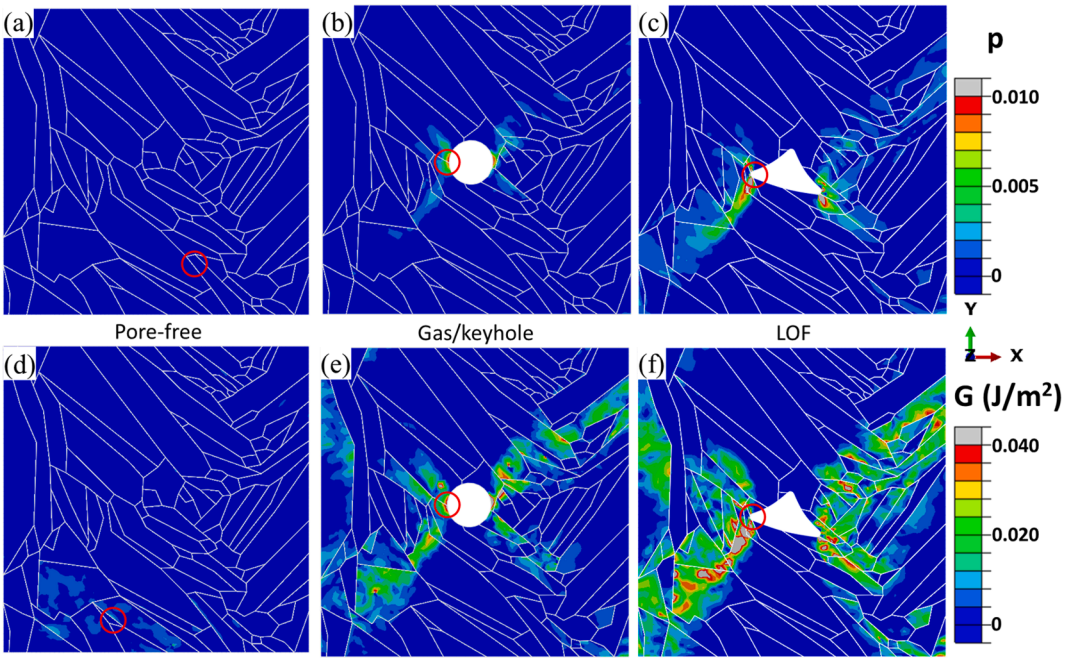

Fig. 5. The distribution of (a-c) accumulated effective plastic strain and (d-e) stored energy density at the 20th cycle for pore-free, gas/keyhole and LOF pores microstructure when $\sigma_{max} = 0.8\sigma_{0.2NP}$. The red circles indicate the location of maximum (a-c) accumulated effective plastic strain and (d-e) stored energy density.

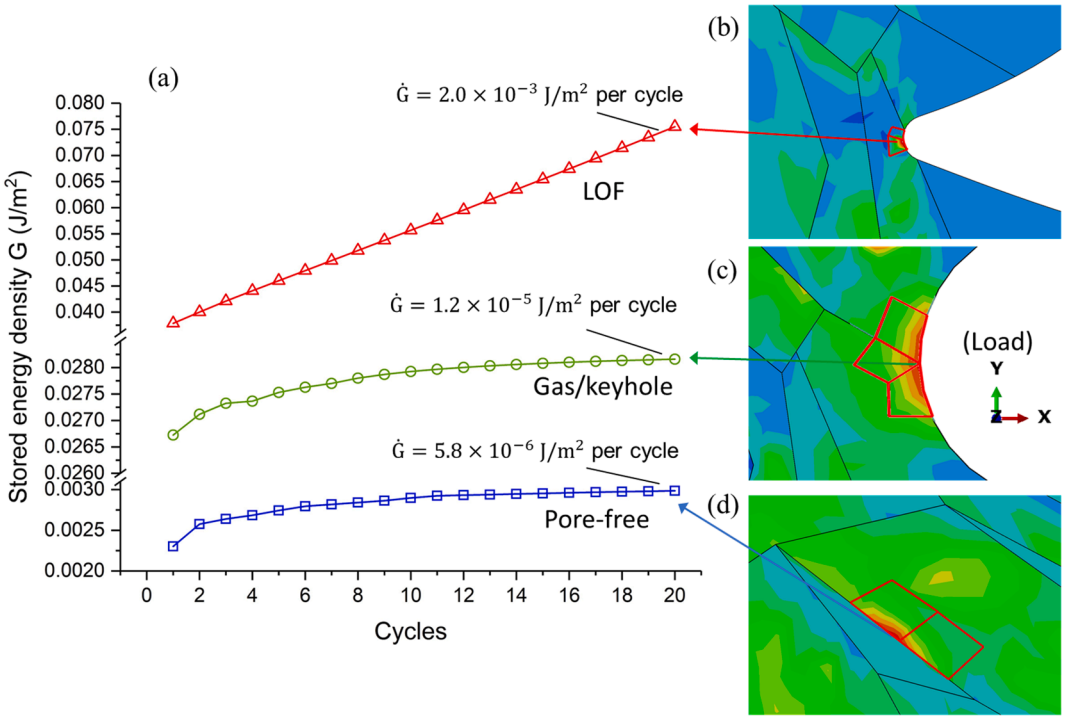

Fig. 6. (a) The evolution of stored energy density G with cycles at applied stress level $\sigma_{max} = 0.8\ \sigma_{0.2NP}$, at critical sites within (b) LOF pore, (c) gas/keyhole pore and (d) pore-free microstructures.

The resulting distributions of accumulated effective plastic strain p and stored energy density G (where the latter drives fatigue crack nucleation) for each model microstructure for stress $\sigma_{max} = 0.8\sigma_{0.2NP}$ are shown in Fig. 5. Clear distinctions in both p and G are observed for the pore-free and differing pored microstructures. For the pore-free microstructure, limited plastic deformation results, and the location of peak p differs from that of G, although they both occur at grain boundaries of grains connected to the bottom surface (which may result from boundary effects).

Substantive increases in both p and G are seen for the pored microstructures, particularly for the LOF pore microstructure and close to the pores, but also influenced by maximum shear directions observed in FCC alloys as a result of multiple slip plane ⟨1 1 0⟩{1 1 1} activation [49]. The inhomogeneous distributions of p and G vary significantly across the sample free surfaces, with the highest values developing predominantly at the boundaries of pores indicated by the red circles in Fig. 5(b-c) and

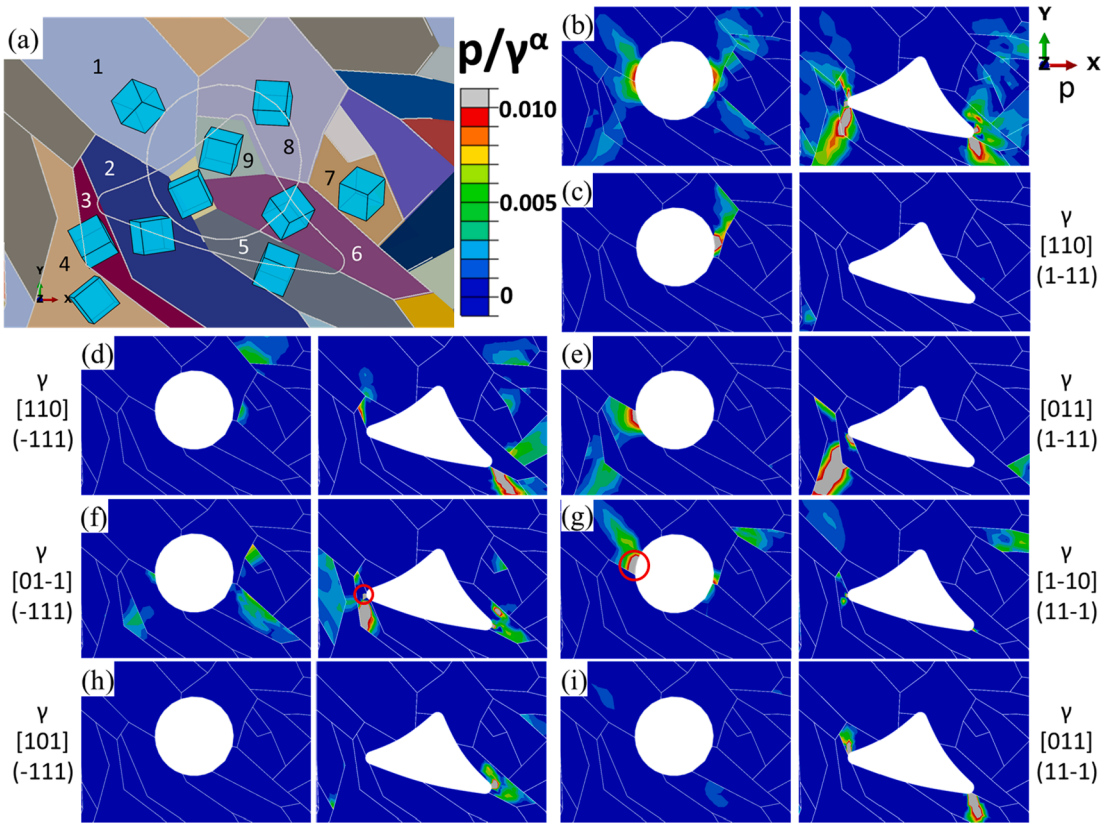

Fig. 7. (a) Region of interest (ROI) showing grain crystallographic orientations and the pore boundaries. Field plots of (b) total accumulated plastic strain and (c-i) accumulated shear strain of dominating slip systems activated for gas/keyhole and LOF pores, respectively, at the 20th cycle and a stress level $\sigma_{max} = 0.8\ \sigma_{0.2NP}$. The red circles in (f) and (g) indicate the slip system with highest value of accumulated shear strain amongst all slip systems in each microstructure.

(e-f), rather than at microstructural inhomogeneities such as grain boundaries as in the pore-free microstructure. These observations show that the presence of pores, regardless of shape, evokes considerably more highly localized slip activation and drives preferential fatigue crack nucleation from the pores.

A quantitative assessment of peak stored energy density evolution with cycles within each microstructure is given in Fig. 6. These sites are those where fatigue crack nucleation is anticipated. The maximum stored energy density in the LOF pore microstructure at the 20th cycle is significantly higher than that of the other two microstructures, and specifically, 2.7 times higher than that for the gas/keyhole pore and 25.3 times higher than for the pore-free microstructure. However, the differences in the cyclic rates of stored energy density evolution $\dot{G}$ are more important showing that for the LOF pore microstructure, it is two orders of magnitude higher than for the gas/keyhole pore microstructure and three orders of magnitude higher than that of the pore-free microstructure. Stored energy density has been shown to be related to fatigue crack nucleation site, and its cyclic rate of increase to the number of cycles to cause nucleation [26,28]. Hence at the stress level ($\sigma_{max} = 0.8\sigma_{0.2NP}$) considered, these substantive differences in G and $\dot{G}$ indicate intensely graded susceptibility to fatigue crack nucleation for the differing pore types in SLM AlSi10Mg, with LOF pores being particularly damaging. These observations correlate well to numerous experimental observations which show that most fatigue cracks in initiate from LOF defects when under cyclic loading [13–16,21,32].

Fig. 6(a) also indicates that the evolution rates of peak energy density for the pore-free and gas/keyhole pore microstructures are higher in the earlier cycles but then reduce to a lower but stable evolution. This occurs even more rapidly for the LOF microstructure, although the steady state evolution rate remains much higher. Littlewood et al. [48,50] observed similar behaviour in GND density and slip accumulation, particularly noting the achievement of steady state before the 20th cycle. It has been argued that the balance between dissipated energy and stored energy is controlled by the establishment of dislocation structures, which generally stabilizes during the first few cycles [26]. Once the dislocation structures are stabilized, the fraction of energy stored in dislocation structures becomes stable, i.e. a low steady rate is reached [26]. As a result, the dislocation structures at the sharp vertices associated with LOF defects are argued to stabilize more rapidly during the first loading cycle, but this requires experimental characterisation to be justified. Another interpretation is that the level of plasticity reached at the first cycle for LOF manifests the nonlinear behaviour including the geometric nonlinearity and physical (elastoplastic) nonlinearity in the vicinity of pores, which leads to the stabilization of stored energy density in the following cycles.

3.1.2. *Slip system activations at pores*

The microstructural region in the vicinity of the pores is examined in order to investigate local slip activation because of its importance to stored energy as a driver of fatigue damage. Fig. 7(a) shows the FCC crystal orientations of (numbered) grains in a region of interest (ROI) containing the pores (marked by the white closed lines). The distributions of accumulated plastic strain p for both the gas/keyhole and LOF pore types is shown in Fig. 7(b). The individual slip system accumulated shear strain γ^{α} for the dominating activated slip systems in the grains surrounding the pores are presented in Fig. 7(c-i). The slip system with the highest shear strain accumulation is [1–10][1–10](11–1) in grain 1 for the gas/keyhole pore microstructure, while it is system [01–1](−111) in grain 3 for LOF pore microstructure, and these locations correspond also to those of maximum G as in Fig. 6(b) and (c).

It is found that there are three strongly activated slip systems local to gas/keyhole pores (Fig. 7(c), (e) and (g)), distributed in the three grains

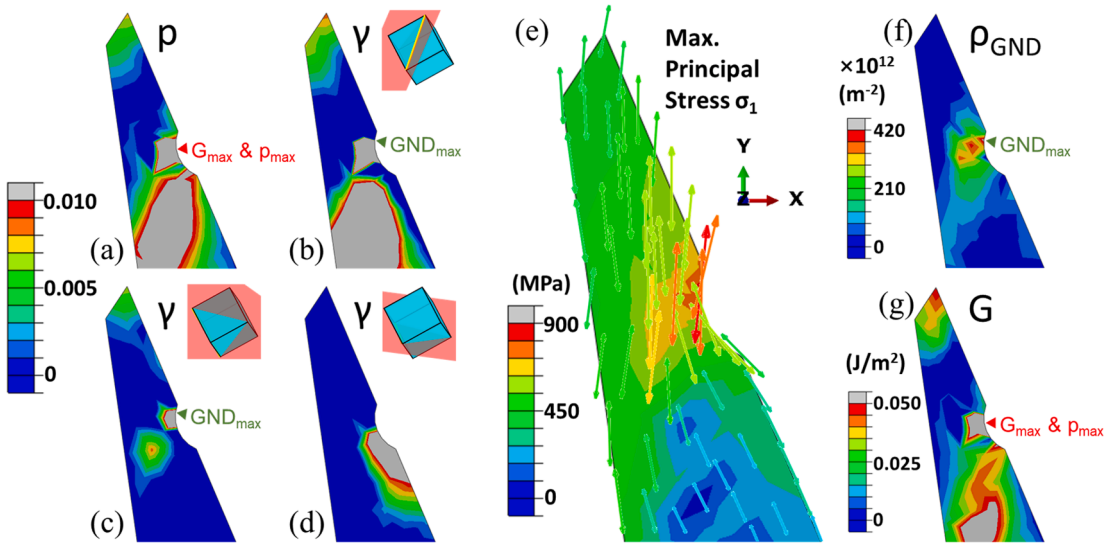

Fig. 8. The distributions of (a) total plastic strain accumulation, accumulated shear of slip systems (b) [01–1](−111), (c) [1–10](11–1) and (d) [011](1–11), (e) maximum principal stress magnitude overlaid with arrows indicating correponding directions, (f) GND density and (g) stored energy density in grain 3 in the LOF pore microstructure at the 20th cycle with stress level $\sigma_{max} = 0.8\ \sigma_{0.2NP}$. The notch at the right side of the grain is the free surface exposed by the LOF.

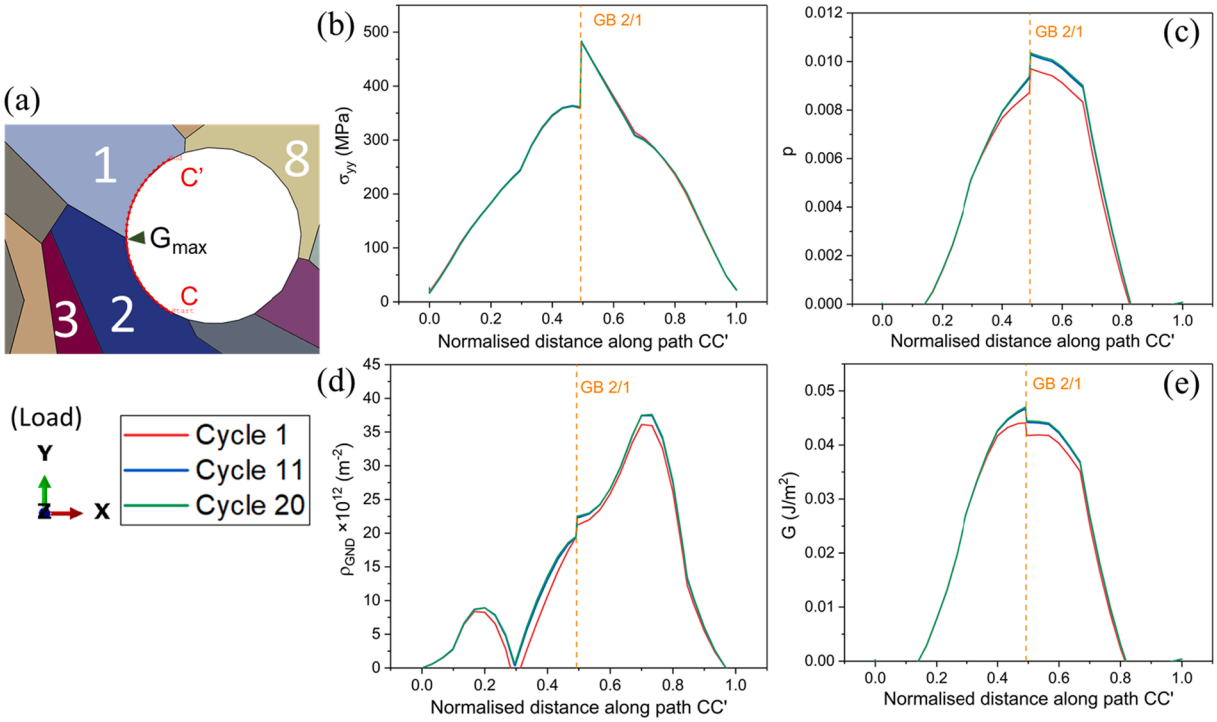

Fig. 9. (a) Path CC' and its surrounding microstructure, and plots of (b) stress in the loading direction, (c) accumulated plastic strain, (d) GND density and (d) stored energy density along the path CC' at cycles 1, 11 and 20, when stress level $\sigma_{max} = 0.8\ \sigma_{0.2NP}$.

which contribute most to the plastic strain development shown in Fig. 7 (b). However, the LOF defect drives more slip system activations and in particular, multiple slip systems are found to be activated in a single grain. For instance, in grain 3 in which the maximum p and G develop, at least three slip systems are activated and exhibit high shear strain accumulations (Fig. 7(e-g)). Similar behaviour is seen in grain 2, adjacent to grain 3, together with grains 5 and 6, which are at the opposite corner of the LOF defect that also drives strain localization.

Grain 3 containing the tip of the LOF defect which develops the maximum p and G is extracted to show the multiple intragranular slip system activations. Magnified views of the distributions of accumulated plastic strain and the accumulated shear of the three activated slip systems in grain 3 are displayed in Fig. 8(a-d). The similarity of distributions of p (Fig. 8(a)) and γ of slip system [01–1](−111) (Fig. 8(b)) suggests that [01–1](−111) is the leading activated slip system contributing to the plasticity occurring at the LOF pore tip.

The multiple intragranular slip system activations arise for several potential reasons. On one hand, the highly symmetric FCC structure and low CRSS of Al result in intrinsically low resistance to slip in AlSi10Mg. On the other hand, the presence of LOF leads to substantial stress concentration at the LOF tips, together with very complex stress state that varies intragranularly, suggested by the spatially inhomogeneous

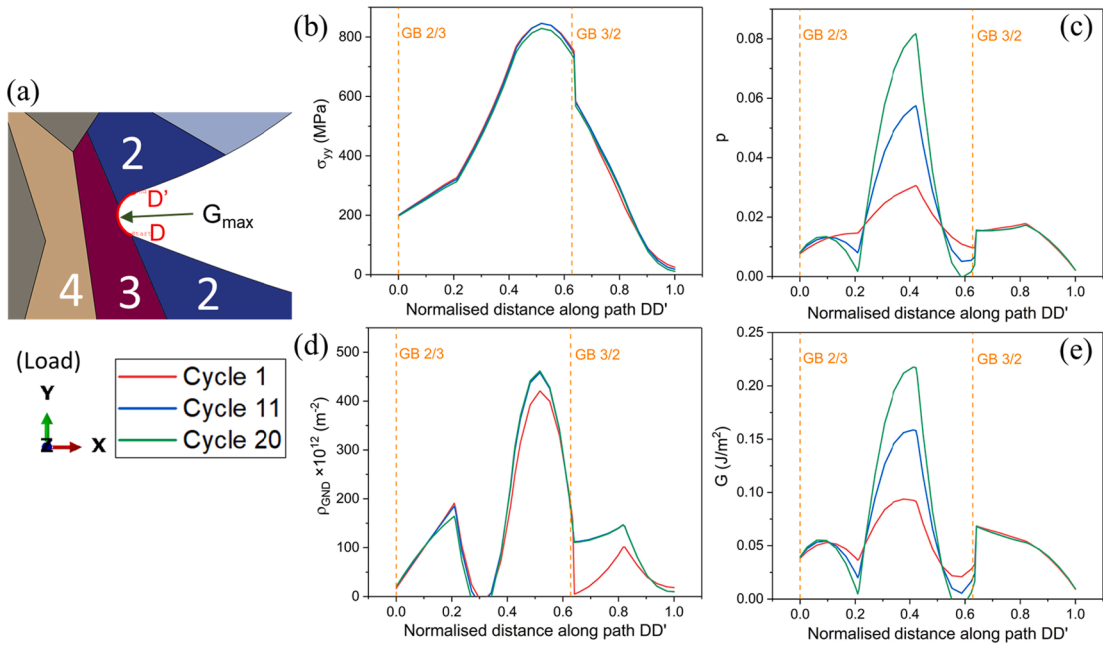

Fig. 10. (a) Path DD' and its surrounding microstructure, and plots of (b) stress in the loading direction, (c) accumulated plastic strain, (d) GND density and (d) stored energy density along the path DD' at cycles 1, 11 and 20, when stress level $\sigma_{max} = 0.8\ \sigma_{0.2NP}$.

distribution of maximum principal stress direction (and magnitude) shown in Fig. 8(e). Furthermore, strong plastic strain localization occurring at LOF tips, shown in Fig. 7(b), may result in lattice rotation. This, together with spatially inhomogeneous stress state, facilitates a range of high local resolved shear stresses on slip systems across the grain, causing activation of multiple slip systems.

Higher numbers of activated slip systems contribute to more plastic strain, and potentially higher GND densities since steeper plastic strain gradients may result. The distribution of GND density in grain 3 at the LOF pore tip is shown in Fig. 8(f). Consequently, higher stored energy density may develop around the LOF pore tips shown in Fig. 8(g) which then drives earlier fatigue crack nucleation in microstructures containing LOF.

A closer examination of critical sites in the two microstructures with pores is provided, along two paths CC' and DD' which are partial perimeters of gas/keyhole and LOF pores, respectively, as shown in Fig. 9 (a) and Fig. 10(a). The stress in the loading direction, accumulated plastic strain, GND density and stored energy density at cycles 1, 11 and 20 along the paths are extracted, as shown in Fig. 9(b-e) and Fig. 10(b-e). The locations of maximum G along each path are highlighted in each of Fig. 9(a) and Fig. 10(a), which are the anticipated fatigue crack nucleation sites based on stored energy density criterion.

The gas/keyhole pore microstructure (Fig. 9) shows that the grain boundary between grain 1 and grain 2 coincides with the geometric stress concentration site, which is at the centre of left half circumference of the pore. The highest stress at this point is 482.1 MPa, much higher than the applied stress level 250.4 MPa. In general, a grain boundary separates two domains with different crystallographic orientations, which may therefore undergo distinct plastic deformation since their major activated slip systems are probably not parallel. This leads to different plastic strain accumulation, and therefore SSD densities, between the two grains under cyclic loading, along with strain gradients at the grain boundary, resulting in GND formation to accommodate the strain gradient. The increase in dislocation density gives rise to higher stresses and potentially higher stored energy density, thus fatigue cracks tend to nucleate at slip localization areas near grain boundaries when no pores or other microstructural heterogeneities are present in the microstructure, which has been demonstrated in both experiments and simulations [23,24,27].

As a consequence, for this microstructure in which a grain boundary and stress concentration site overlap, it is expected that this site corresponds to the maximum of σ_{yy}, p, ρ_{GND} and G, as shown in Fig. 9(b-e), except for the GND density distribution where the maximum develops within the bulk of grain 1. In fact, it is found that this site of maximum ρ_{GND} coincides exactly with the boundary of the domain of high accumulated shear strain of slip system [1–10](11–1) in grain 1, as shown in Fig. 7(g). This high GND density arises to accommodate the high strain gradient within grain 1, which is further indicated by the large gradient in Fig. 9(c) at 0.7 of path CC'. Nonetheless, a clear change in GND density still exists at the grain boundary, just as for σ_{yy}, p and G. Since stored energy density is an integrated result of stress, plastic strain and dislocation densities, the maximum location of G does not necessarily coincide with any one of σ_{yy}, p or ρ_{GND}.

The LOF pore microstructure (Fig. 10) shows somewhat different behaviour since the maximum values of all four quantities no longer develop at grain boundaries as opposed to the case for gas/keyhole pore microstructure, largely because the geometric stress concentration site does not overlap with a grain boundary. The maximum σ_{yy} at the tip of the LOF increases to 846.0 MPa according to Fig. 10(b), which is 75.5% higher than that of the gas/keyhole pore and 3.4 times the applied stress level. The dominating feature driving the increase in stress is the stress concentration associated with the higher curvature of the sharp corner of the LOF, as compared to the circular gas/keyhole pore. This extreme stress concentration, together with low CRSS, spatially inhomogeneous stress state and developing lattice rotation, results in multiple slip system activations in grain 3 shown in Fig. 8(b-d). Therefore, very intense plastic deformation localizes at the corner of the LOF, indicated by an up to 8.2% plastic strain accumulation in Fig. 10(c), which is nearly an order of magnitude higher than that at the gas/keyhole pore.

The maximum GND density developing mid-way along path DD' shown in Fig. 10(d), which is 4.6×10^{14} m^{-2}, is an order of magnitude higher than that for the gas/keyhole pore. The extremely high value of GND density indicates strongly localized plastic strain gradients exist at the LOF pore tip. The site where high GND density occurs is marked in Fig. 8(b, c, f), and is actually found to correspond to the boundary of the domain with high plastic strain, which is contributed by two major slip systems activated in grain 3: [01–1](−111) (Fig. 8(b)) and [1–10](11–1) (Fig. 8(c)). Independent evidence suggests that multiple

intragranular slip system activations lead to local increase in GND density [34,51]. Thus, this high value of ρ_{GND} at the tip of the LOF is the result of the interactions between differing intragranular slip systems inducing very steep strain gradients in grain 3. Moreover, the highest SSD density along DD' is found to be four orders of magnitude lower than the GND density, indicating the dislocation structures are dominated by GNDs arising from the first cycle (Fig. 10(d)). The substantial increase in ρ_{GND} in grain 3 at the LOF pore tip results in local elevation in stresses due to latent hardening, which eventually contributes to higher stored energy density level than that of gas/keyhole pore microstructure.

Furthermore, large increases in p and G between cycles 11 and 20 occur as shown in Fig. 10(c) and (e), suggesting high and constant evolution rates corresponding to the rapid linear growth in stored energy shown in Fig. 6. The similar distributions and evolution of p and G manifest that the rapid accumulation of localized plastic strain induced by the LOF is prominent that it dominates the evolution of stored energy density during cyclic loading at the LOF pore tip.

Hence, it is argued that the pronounced increase in GND density due to multiple intragranular slip system activations occurring at the sharp corners of LOF is an important mechanistic driver that pushes up local stresses and stored energy density in the early loading cycles. However, it is the rapid accumulation of plastic strain that dominates and accounts for the rapid linear growth in stored energy density during subsequent cyclic loading. These two aspects, involving roles of both GNDs and plastic strain, establish the high stored energy density and provide the mechanistic understanding of the strong sensitivity of fatigue crack nucleation to LOF pores in SLM components, as well as the more detrimental effect of LOF as opposed to gas/keyhole pores in SLM alloys.

3.1.3. Shift of critical site from gas/keyhole pore to microstructural heterogeneities

A particular phenomenon of interest is that when stress levels σ_{max} higher than $0.8\sigma_{0.2NP}$ are applied to the gas/keyhole pore microstructure, the microstructural location with maximum G and $\dot{G}$, i.e. the critical site for fatigue crack nucleation, shifts from pore boundary to grain boundary within the microstructure removed from the pore. This observation is demonstrated in Fig. 11.

It is observed that with increasing stress level σ_{max} from $0.7\sigma_{0.2NP}$ to $1.0\sigma_{0.2NP}$, the maximum p always develops at the pore boundary (Fig. 11 (a-d)), whereas the maximum G shifts from pore boundary to a grain boundary triple junction away from the pore when σ_{max} reaches $0.9\sigma_{0.2NP}$ (Fig. 11(e-h)). At the stress level of $\sigma_{max} = 0.7\sigma_{0.2NP}$, the plastic deformation is mainly confined in the vicinity of the gas/keyhole pore and does not extend across the diagonals of the microstructure (Fig. 11 (a)), thus the shear band formation is relatively weak. When σ_{max} increases to $0.8\sigma_{0.2NP}$, shear bands start to appear, as shown in Fig. 11(b), and the microstructural inhomogeneities within the shear band start to accumulate plastic strain, dislocation structures, and hence dislocation-stored energy. In other words, this is when microstructural inhomogeneities start to have stronger influence on the critical site for fatigue crack nucleation. However, the critical site has not changed at this stress level since G and $\dot{G}$ have not surpassed those magnitudes at the pore boundary. When the applied σ_{max} increases up to $0.9\sigma_{0.2NP}$ and above, G and $\dot{G}$ at the grain boundary near the upper right corner of the microstructure circled in Fig. 11(g-h) exceed other locations, making this site more prone to fatigue crack nucleation than at the gas/keyhole pore.

The shift of critical fatigue crack nucleation site at higher stresses suggests that when the applied cyclic stress level is sufficiently high for severe shear band formation, fatigue crack nucleation is likely to be more sensitive to microstructural inhomogeneities, such as grain boundaries in this case, than a spherical gas/keyhole pore. And the higher the stress level, the higher the possibility for microstructural features to become critical sites.

Grain boundaries are often found to be the critical sites for fatigue crack nucleation in microstructures with no pores [23,26,27], and they often correspond to sites with high plastic strain accumulation or dislocation density. In this case however, the critical site at the grain boundary shown in Fig. 11(g-h) does not correspond to any maximum of σ_{yy}, p or ρ_{GND} within the microstructure. In particular, the GND density at this site is found to be merely 3.6% of the GND density at the pore boundary after 20 cycles, while the stress and plastic strain are 73.8% and 37.7% respectively. However, these conditions give rise to the highest G at this site. An interpretation at this grain boundary is that the low dislocation density corresponds to longer slip lengths and thus

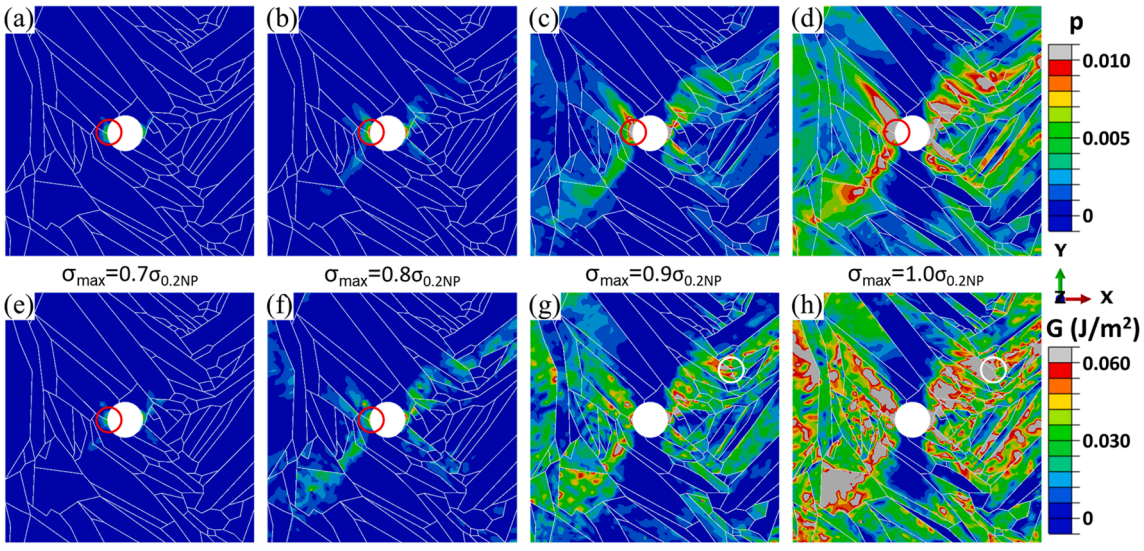

Fig. 11. The distributions of plastic strain accumulation and stored energy density at the 20th cycle in gas/keyhole pore microstructure at different cyclic loading levels: (a,e) $\sigma_{max} = 0.7\sigma_{0.2NP}$, (b,f) $\sigma_{max} = 0.8\sigma_{0.2NP}$, (c,g) $\sigma_{max} = 0.9\sigma_{0.2NP}$, and (d,h) $\sigma_{max} = 1.0\sigma_{0.2NP}$. The red or white circles indicate the locations of maximum p or G within each microstructure.

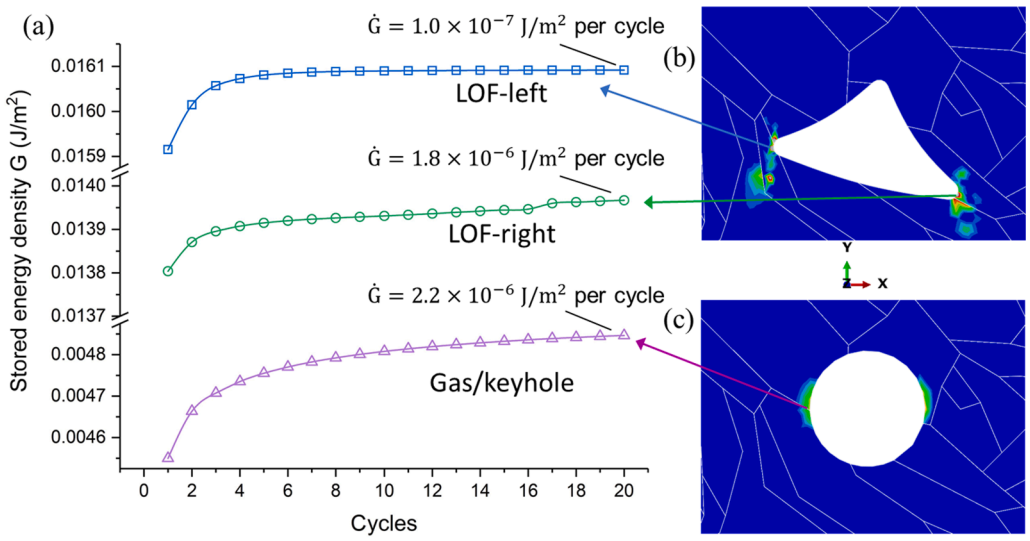

Fig. 12. (a)The evolution of stored energy density against loading cycles at locations with high G as shown in the distributions within the microstructure containing (b) LOF pore and (c) gas/keyhole pore, for low applied stress ($\sigma_{max} = 0.5\sigma_{0.2NP}$).

higher energy storage volume ΔV_s, resulting in higher $\dot{G}$.

Furthermore, observations from Fig. 5 suggest that the shear band formation is enhanced by the presence of a pore in the microstructure. As a consequence, despite fatigue crack nucleation being more sensitive to microstructural heterogeneities than gas/keyhole pores at circumstances where very high cyclic load is applied, the microstructural feature could not in its own right lead to the shift of critical site away from the pore. The pore-induced shear band formation is also considered necessary for the shift of critical site to occur, so the pores here still play a role.

A critical size for spherical pores has been suggested below which the pore is not as detrimental as other microstructural features in driving fatigue cracks [30,31]. This observation is reflected in terms of stored energy density here for gas/keyhole pores. Hot isostatic pressing (HIP) has been employed to effectively lower or even eliminate the porosity in AM components, in spite of it leading to other potentially more damaging microstructural features [52]. Fatigue cracks have been observed to initiate from HIPed sample surfaces where no obvious defects are present, such that local microstructures are suspected to play a major role [53,54]. This may result from high stress levels in which the coupling effect of small spherical pores and microstructural heterogeneities determines the critical site removed from the pore itself, similar to the results discussed above.

3.2. Fatigue behaviour at low stress levels

The local mechanical responses at low stress levels in the vicinity of the pores are also investigated for the two microstructures with pores. The stress level $\sigma_{max} = 0.5\sigma_{0.2NP}$ is selected to be representative of low stress level. Fig. 12 shows the evolutions of stored energy associated with the differing pore types at the low applied stress of $0.5\sigma_{0.2NP}$. Both gas/keyhole and LOF pores drive higher stored energy densities, suggesting preferential fatigue crack nucleation at these sites as opposed to other microstructural features at low stress levels. But the critical site for predicted fatigue crack nucleation at the LOF shifts from its left corner (that at high stress levels) to the right corner, because of very low stored energy rate at the left corner, shown in Fig. 12(a).

The highest stored energy in the gas/keyhole pore microstructure at 20 cycles is below that corresponding to the LOF pore, but it transpires that the rates of evolution in subsequent cycles at the right corner of LOF are about equal to or lower than those for gas/keyhole pores. This is contrary to the observations at high stress levels, such that fatigue crack nucleation may be achieved (depending on the critical stored energy density) in the gas/keyhole pore microstructure prior to, or at the similar number of cycles, as that for the LOF pore.

The local slip system activation at low stress for both gas/keyhole and LOF pores is examined in order to reveal the mechanistic reason for the contrary. The number of activated slip systems at the gas/keyhole pore remains unchanged for low applied stress compared to high stress. However, at the left corner of the LOF pore, slip system [0 1 1](1–11) in grain 3 (which is activated at high stress levels in Fig. 8(d)) develops very limited slip at low stress levels. As a consequence, less slip system interactions result in lower GND density and stress which then reduce the stored energy density rate to below that of the gas/keyhole pore (as well as the right corner of the LOF). This in turn leads to longer fatigue crack nucleation life for the LOF pore microstructure.

3.3. Fatigue life assessment

The stored energy density criterion not only enables the capture of the site of fatigue crack nucleation, but also provides the cycles required to nucleate of fatigue cracks [33,34]. With the stored energy density rate $\dot{G}$ obtained at the critical microstructural sites, the cycles to fatigue crack nucleation may then be obtained assuming that the evolution of G has reached a steady state within 20 cycles for each microstructure, which has been demonstrated in Fig. 6. With all G and $\dot{G}$ at critical sites obtained for all three microstructures (pore-free, gas/keyhole pore and LOF pore) at different stress levels, the cycles to fatigue crack nucleation at each condition may then be calculated. Thus, the link between macroscopic cyclic loading and cycles to fatigue crack nucleation can be extracted, that is, the S-N curve, which is commonly used for evaluating fatigue performance for engineering alloys.

The remaining quantity which determines cycles to failure is the critical stored energy density G_c for the AlSi10Mg. From Eq. (13), the contribution to stored energy can be written in terms of energy stored in the early cycles as $\dot{G}$ evolves, together with that stored subsequent to a steady state evolution rate of $\dot{G}$ being established. With experimentally determined cycles to failure for given loading conditions, this then gives critical stored energy density to be:

$$G_c = \int \dot{G} dN = G_{20sim} + \dot{G}_{20sim}(N_{exp} - 20) \quad (16)$$

in which G_{20sim} and $\dot{G}_{20sim}$ represent the stored energy density and its rate corresponding to the critical site within the microstructure at the 20th cycle, respectively. N_{exp} ($\gg 20$) is the number of cycles taken from the experiment in [47] for the SLM AlSi10Mg alloy built in the vertical direction which makes it applicable to inferring G_c for the current microstructure. This CPFE model microstructure is subjected to the same fatigue loading condition as that in [47], where one of the experimental applied stress levels $\sigma_{max} = 189$ MPa is close to the stress level of $\sigma_{max} = 0.6\sigma_{0.2NP} = 187.7$ MPa considered above. This stress gives rise to an observed fatigue life of 32,693 cycles to failure.

The fatigue cracks were reported to consistently initiate from large irregular sub-surface defects revealed by machining [47], so that it is reasonable to assume the sample condition for the extracted experimental data corresponds to a microstructure containing LOF pore. The model microstructure then gives appropriate values for G_{20sim} and $\dot{G}_{20sim}$ such that Eq. (16) then provides G_c for SLM AlSi10Mg to be 0.64345 J/m^2. It is noted, however, that not considering the time period of short crack growth and subsequent crack propagation would result in less accuracy of predicting fatigue lifetime for specific stress levels. In addition, the slightly different processing parameters used to build the fatigue samples in [47] may cause minor variations in local microstructures compared to the models from [41]. The microstructural differences could usefully be investigated using the crystal plasticity modelling approach presented in future work. However, here we focus on qualitative comparisons of the fatigue life reduction resulting from the differing pore types, rather than the accuracy of fatigue lifetime evaluations.

Having determined G_c, the predicted cycles to fatigue crack nucleation N_{sim} for each microstructural model subjected to an appropriate range of stress levels may be then determined from:

$$N_{sim} = \frac{G_c - G_{20sim}}{\dot{G}_{20sim}} + 20 \quad (17)$$

Predicted S-N data points showing applied cyclic peak stress σ_{max} versus predicted number of cycles to fatigue crack nucleation N_{sim} for SLM AlSi10Mg are shown in Fig. 13. The bounds for predicted cycles to failure are included.

The impact of differing pore types on predicted fatigue crack nucleation life is evident in Fig. 13. The fatigue limit for the pore-free microstructure is found to be about 219.1 MPa, whereas fatigue limits for the microstructures with pores have not been established. From the model predicted results, very clear reductions in fatigue life of microstructures containing gas/keyhole and LOF pores result compared to the pore-free microstructure, with the latter giving orders of magnitude of higher reductions at high applied stresses ($\sigma_{max} \geq 0.6\sigma_{0.2NP}$). This demonstrates the pronounced detriment of pores, especially LOF, to the fatigue performance of SLM AlSi10Mg. This also reflects the orders of magnitude higher stored energy rate developing at the LOF pore tips

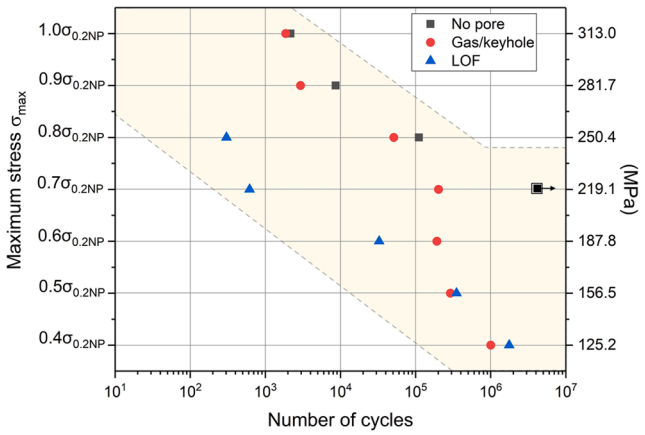

Fig. 13. Maximum applied cyclic stress against number of cycles to fatigue crack nucleation predicted by CPFE modelling based on a stored energy density criterion for all three microstructures. The symbol with an arrow indicates that the fatigue limit is reached. The shaded region indicates the estimated range for predicted cycles to fatigue failure.

compared with pore-free and gas/keyhole pore microstructure shown in Fig. 6. In addition, at very high stress levels ($\sigma_{max} \geq 0.8\sigma_{0.2NP}$), the fatigue crack nucleation lives of pore-free and gas/keyhole pore microstructures tend to converge. This reflects the increasing influence of (non-pore) microstructural features with increasing applied stresses on driving fatigue cracks in gas/keyhole pore microstructures, resulting from earlier fatigue crack nucleation at grain boundaries away from gas/keyhole pore at very high stress levels. As the applied stress is reduced ($\sigma_{max} \leq 0.5\sigma_{0.2NP}$), however, the damaging effects of the LOF pore compared with the gas/keyhole pore diminish such that their fatigue lifetimes converge, resulting from the weakened slip system interactions at the LOF tips.

The changes in predicted fatigue lifetime with respect to stress levels reflect not simply the direct influence of applied stress, but also the change in mechanism taking place as a result of the differing stress, through altering local micromechanical responses subjected to cyclic loading.

However, unexpected decrease in fatigue life is noticed for gas/keyhole pore microstructure when applied stress σ_{max} is reduced from $0.7\sigma_{0.2NP}$ to $0.6\sigma_{0.2NP}$. For most crystal plasticity models, there is a clear monotonic predicted fatigue lifetime tendency with regards to strain or stress amplitude [33,55], such that this observation suggests multiple realizations of microstructure would be useful to improve the accuracy of lifetime predictions and to show if the anomaly persists. Moreover, there are clear differences between the fatigue lives for the LOF results from experiment and model calculation. For the latter, compared with experiment, shorter fatigue lives are obtained at high stress and somewhat longer lives at low stress such that the predicted sensitivity of LOF pores to stress does not reflect that seen in experiment with higher sensitivity resulting from the model calculations. The model results are based on an assumed worst-case geometry for a single LOF, whereas those in the experiment are not reported. This strongly suggests that studies of LOF pore morphology and distribution would be useful to carry out and may explain the differing gradients of stress versus cycles observed.

4. Conclusions

A crystal plasticity finite element modelling approach has been adopted to analyse fatigue crack nucleation behaviour in SLM AlSi10Mg resulting from differing pore types: idealized gas/keyhole and LOF pores. The distributions of stress, accumulated plastic strain, GND density and stored energy density are examined in detail in each model microstructure at different applied stress levels, particularly in the vicinity of pores. The life to fatigue crack nucleation is quantified for comparative study based on the stored energy density criterion and S-N curves are provided. The roles of pores, microstructures and applied stress levels as well as their interactions are addressed. The major conclusions are:

- The high sensitivity of fatigue crack nucleation to pores in SLM AlSi10Mg is well captured by the CPFE models predicted by the stored energy density criterion, demonstrating preferred nucleation sites at the boundaries of gas/keyhole and LOF pores.
- At high stress levels, high stored energy density at the LOF pore tips in the early cycles is dominated by multiple intragranular slip system activations, leading to intense local GND density increase and high local stresses. Subsequent steady cyclic increase of stored energy density is controlled by plastic strain accumulation.
- Applied cyclic peak stress affects local micromechanical responses, resulting in different mechanisms for fatigue crack nucleation. Shear banding induced by gas/keyhole pores at very high stress make fatigue cracks more sensitive to microstructural inhomogeneities away from the pores. At low stress levels, reduced slip system interactions at the LOF pore tips moderate local stored energy density rates.
- Both gas/keyhole and LOF pores decrease predicted fatigue life for SLM AlSi10Mg, with the LOF pore resulting in orders of magnitude in reduction at high cyclic peak stress. Fatigue lives of gas/keyhole pore and pore-free microstructures converge at high stress levels. LOF pore microstructures exhibit similar or longer predicted fatigue life than that for gas/keyhole pore at low stress levels.

Declaration of Competing Interest

The authors declare that they have no known competing financial interests or personal relationships that could have appeared to influence the work reported in this paper.

Appendix

A convergence study is conducted to ensure the mesh density is high enough for the models to produce reliable mechanical responses, through applying monotonic loading to the pore-free microstructure using three different number of elements, 3388, 5604 and 7464. The macroscopic stress–strain responses, together with distributions of σ_{yy}, p, ρ_{GND} and G along the horizontal line in the middle of the front free surface under three meshing conditions are displayed in Fig. A. The macroscopic stress–strain curves for the three meshing conditions are found to be basically overlapping, whereas deviations exist in σ_{yy}, p, ρ_{GND} and G along path AA'. The differences in the peak values of these quantities between using 5604 and 7464 elements are within 10%, while the computation time when meshing with 7464 elements increases significantly. Therefore, it is reasonable to believe that the mechanical response has converged when using 5604 elements with approximate global mesh size of 2 μm for the CPFE model, which also saves computational resources. Similar meshing conditions are employed for later simulations of microstructures with gas/keyhole pore and LOF.

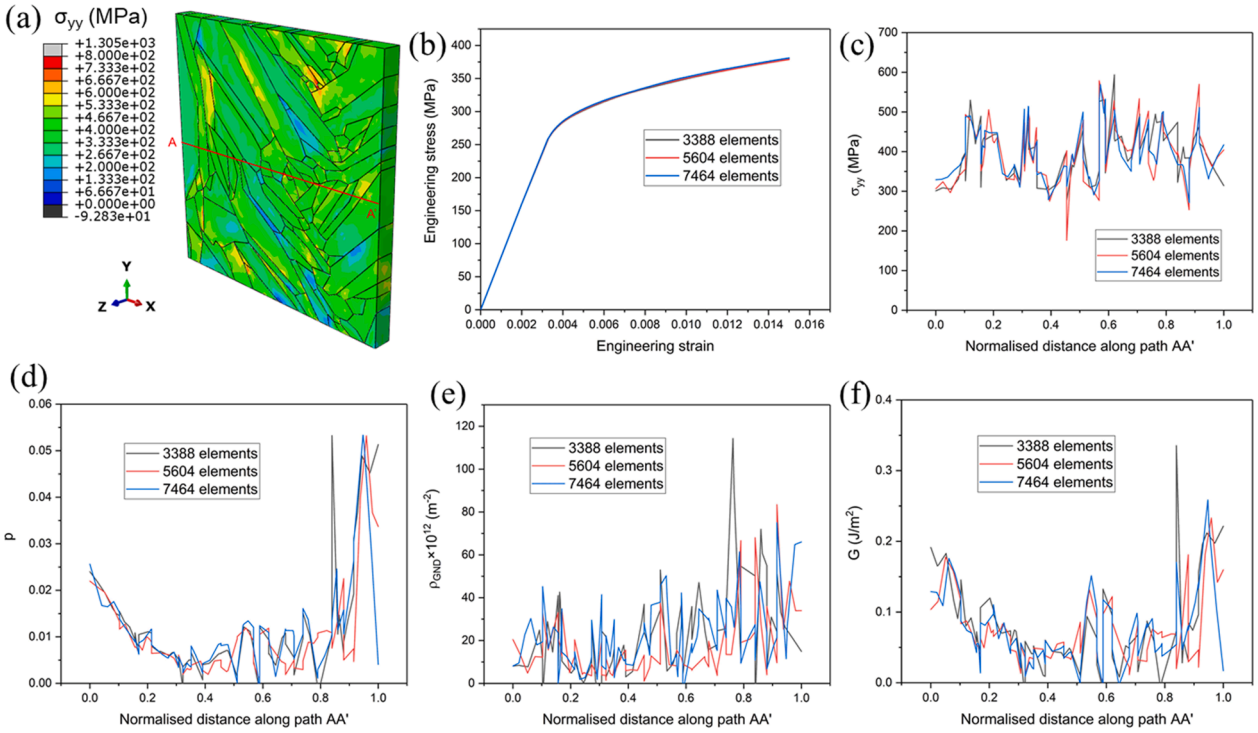

Fig. A. . Results for meshing convergence study: (a) the distribution of stress in the loading direction using 5604 elements after monotonic loading to 1.5% global strain, with the path AA' shown on the model, (b) the macroscopic stress–strain responses for three meshing densities and (c-f) the σ_{yy}, p, ρ_{GND} and G distributions, respectively, along path AA' for three meshing conditions.

References

[1] DebRoy T, Wei HL, Zuback JS, Mukherjee T, Elmer JW, Milewski JO, et al. Additive manufacturing of metallic components – Process, structure and properties. Prog Mater Sci 2018;92:112–224. https://doi.org/10.1016/j.pmatsci.2017.10.001.

[2] Frazier WE. Metal Additive Manufacturing: A Review. J Mater Eng Perform 2014; 23:1917–28. https://doi.org/10.1007/s11665-014-0958-z.

[3] Gu DD, Meiners W, Wissenbach K, Poprawe R. Laser additive manufacturing of metallic components: materials, processes and mechanisms. Int Mater Rev 2013; 57:133–64. https://doi.org/10.1179/1743280411y.0000000014.

[4] Aboulkhair NT, Everitt NM, Ashcroft I, Tuck C. Reducing porosity in AlSi10Mg parts processed by selective laser melting. Addit Manuf 2014;1–4:77–86. https://doi.org/10.1016/j.addma.2014.08.001.

[5] Sanaei N, Fatemi A. Defects in additive manufactured metals and their effect on fatigue performance: A state-of-the-art review. Prog Mater Sci 2020. https://doi.org/10.1016/j.pmatsci.2020.100724.

[6] Cunningham R, Zhao C, Parab N, Kantzos C, Pauza J, Fezzaa K, et al. Keyhole threshold and morphology in laser melting revealed by ultrahigh-speed x-ray imaging. Science 2019;363:849–52. https://doi.org/10.1126/science.aav4687.

[7] Pham MS, Dovgyy B, Hooper PA, Gourlay CM, Piglione A. The role of side-branching in microstructure development in laser powder-bed fusion. Nat Commun 2020;11:749. https://doi.org/10.1038/s41467-020-14453-3.

[8] Aboulkhair NT, Simonelli M, Parry L, Ashcroft I, Tuck C, Hague R. 3D printing of Aluminium alloys: Additive Manufacturing of Aluminium alloys using selective laser melting. Prog Mater Sci 2019;106. https://doi.org/10.1016/j.pmatsci.2019.100578.

[9] Kempen K, Thijs L, Van Humbeeck J, Kruth JP. Processing AlSi10Mg by selective laser melting: parameter optimisation and material characterisation. Mater Sci Technol 2014;31:917–23. https://doi.org/10.1179/1743284714y.0000000702.

[10] Zhang H, Gu D, Dai D, Ma C, Li Y, Cao M, et al. Influence of heat treatment on corrosion behavior of rare earth element Sc modified Al-Mg alloy processed by selective laser melting. Appl Surf Sci 2020;509. https://doi.org/10.1016/j.apsusc.2020.145330.

[11] Dunne FPE, Wilkinson AJ, Allen R. Experimental and computational studies of low cycle fatigue crack nucleation in a polycrystal. Int J Plast 2007;23:273–95. https://doi.org/10.1016/j.ijplas.2006.07.001.

[12] Yeratapally SR, Lang C, Glaessgen EH. A computational study to investigate the effect of defect geometries on the fatigue crack driving forces in powder-bed AM materials, in: AIAA Scitech 2020 Forum, 2020.

[13] Romano S, Patriarca L, Foletti S, Beretta S. LCF behaviour and a comprehensive life prediction model for AlSi10Mg obtained by SLM. Int J Fatigue 2018;117:47–62. https://doi.org/10.1016/j.ijfatigue.2018.07.030.

[14] Brandl E, Heckenberger U, Holzinger V, Buchbinder D. Additive manufactured AlSi10Mg samples using Selective Laser Melting (SLM): Microstructure, high cycle fatigue, and fracture behavior. Mater Des 2012;34:159–69. https://doi.org/10.1016/j.matdes.2011.07.067.

[15] Jian ZM, Qian GA, Paolino DS, Tridello A, Berto F, Hong YS. Crack initiation behavior and fatigue performance up to very-high-cycle regime of AlSi10Mg fabricated by selective laser melting with two powder sizes. Int J Fatigue 2021;143. https://doi.org/10.1016/j.ijfatigue.2020.106013.

[16] Wu Z, Wu S, Bao J, Qian W, Karabal S, Sun W, et al. The effect of defect population on the anisotropic fatigue resistance of AlSi10Mg alloy fabricated by laser powder bed fusion. Int J Fatigue 2021;151. https://doi.org/10.1016/j.ijfatigue.2021.106317.

[17] Mower TM, Long MJ. Mechanical behavior of additive manufactured, powder-bed laser-fused materials. Mater Sci Eng, A 2016;651:198–213. https://doi.org/10.1016/j.msea.2015.10.068.

[18] du Plessis A, Yadroitsava I, Yadroitsev I. Effects of defects on mechanical properties in metal additive manufacturing: A review focusing on X-ray tomography insights. Mater Des 2020;187. https://doi.org/10.1016/j.matdes.2019.108385.

[19] Murakami Y, Endo M. Effects of defects, inclusions and inhomogeneities on fatigue strength. Int J Fatigue 1994;16:163–82. https://doi.org/10.1016/0142-1123(94)90001-9.

[20] Beretta S, Romano S. A comparison of fatigue strength sensitivity to defects for materials manufactured by AM or traditional processes. Int J Fatigue 2017;94: 178–91. https://doi.org/10.1016/j.ijfatigue.2016.06.020.

[21] Romano S, Brückner-Foit A, Brandão A, Gumpinger J, Ghidini T, Beretta S. Fatigue properties of AlSi10Mg obtained by additive manufacturing: Defect-based modelling and prediction of fatigue strength. Eng Fract Mech 2018;187:165–89. https://doi.org/10.1016/j.engfracmech.2017.11.002.

[22] McDowell DL, Dunne FPE. Microstructure-sensitive computational modeling of fatigue crack formation. Int J Fatigue 2010;32:1521–42. https://doi.org/10.1016/j.ijfatigue.2010.01.003.

[23] Sweeney CA, Vorster W, Leen SB, Sakurada E, McHugh PE, Dunne FPE. The role of elastic anisotropy, length scale and crystallographic slip in fatigue crack nucleation. J Mech Phys Solids 2013;61:1224–40. https://doi.org/10.1016/j.jmps.2013.01.001.

[24] Sangid MD. The physics of fatigue crack initiation. Int J Fatigue 2013;57:58–72. https://doi.org/10.1016/j.ijfatigue.2012.10.009.

[25] Korsunsky AM, Dini D, Dunne FPE, Walsh MJ. Comparative assessment of dissipated energy and other fatigue criteria. Int J Fatigue 2007;29:1990–5. https://doi.org/10.1016/j.ijfatigue.2007.01.007.

[26] Wan VVC, MacLachlan DW, Dunne FPE. A stored energy criterion for fatigue crack nucleation in polycrystals. Int J Fatigue 2014;68:90–102. https://doi.org/10.1016/j.ijfatigue.2014.06.001.

[27] Chen B, Jiang J, Dunne FPE. Microstructurally-sensitive fatigue crack nucleation in Ni-based single and oligo crystals. J Mech Phys Solids 2017;106:15–33. https://doi.org/10.1016/j.jmps.2017.05.012.

[28] Chen B, Jiang J, Dunne FPE. Is stored energy density the primary meso-scale mechanistic driver for fatigue crack nucleation? Int J Plast 2018;101:213–29. https://doi.org/10.1016/j.ijplas.2017.11.005.

[29] Wilson D, Zheng Z, Dunne FPE. A microstructure-sensitive driving force for crack growth. J Mech Phys Solids 2018;121:147–74. https://doi.org/10.1016/j.jmps.2018.07.005.

[30] Prithivirajan V, Sangid MD. The role of defects and critical pore size analysis in the fatigue response of additively manufactured IN718 via crystal plasticity. Mater Des 2018;150:139–53. https://doi.org/10.1016/j.matdes.2018.04.022.

[31] Sangid MD, Ravi P, Prithivirajan V, Miller NA, Kenesei P, Park J-S. ICME Approach to Determining Critical Pore Size of IN718 Produced by Selective Laser Melting. Jom 2019;72:465–74. https://doi.org/10.1007/s11837-019-03910-0.

[32] Zhang W, Hu Y, Ma X, Qian G, Zhang J, Yang Z, et al. Very-high-cycle fatigue behavior of AlSi10Mg manufactured by selected laser melting: Crystal plasticity modeling. Int J Fatigue 2021;145. https://doi.org/10.1016/j.ijfatigue.2020.106109.

[33] Chen B, Janssens KGF, Dunne FPE. Role of geometrically necessary dislocation density in multiaxial and non-proportional fatigue crack nucleation. Int J Fatigue 2020;135. https://doi.org/10.1016/j.ijfatigue.2020.105517.

[34] Lu X, Dunne FPE, Xu Y. A crystal plasticity investigation of slip system interaction, GND density and stored energy in non-proportional fatigue in Nickel-based superalloy. Int J Fatigue 2020;139. https://doi.org/10.1016/j.ijfatigue.2020.105782.

[35] Dunne FPE, Rugg D, Walker A. Lengthscale-dependent, elastically anisotropic, physically-based hcp crystal plasticity: Application to cold-dwell fatigue in Ti alloys. Int J Plast 2007;23:1061–83. https://doi.org/10.1016/j.ijplas.2006.10.013.

[36] Hodowany J, Ravichandran G, Rosakis AJ, Rosakis P. Partition of plastic work into heat and stored energy in metals. Exp Mech 2000;40:113–23. https://doi.org/10.1007/BF02325036.

[37] Wu JH, Tsai WY, Huang JC, Hsieh CH, Huang G-R. Sample size and orientation effects of single crystal aluminum. Mater Sci Eng, A 2016;662:296–302. https://doi.org/10.1016/j.msea.2016.03.076.

[38] Lu G, Kioussis N, Bulatov VV, Kaxiras E. Generalized-stacking-fault energy surface and dislocation properties of aluminum. Physical Review B 2000;62:3099–108. https://doi.org/10.1103/PhysRevB.62.3099.

[39] Zhang Z. Micromechanistic study of textured multiphase polycrystals for resisting cold dwell fatigue. Acta Mater 2018;156:254–65. https://doi.org/10.1016/j.actamat.2018.06.033.

[40] Hu P, Liu Y, Zhu Y, Ying L. Crystal plasticity extended models based on thermal mechanism and damage functions: Application to multiscale modeling of aluminum alloy tensile behavior. Int J Plast 2016;86:1–25. https://doi.org/10.1016/j.ijplas.2016.07.001.

[41] Thijs L, Kempen K, Kruth J-P, Van Humbeeck J. Fine-structured aluminium products with controllable texture by selective laser melting of pre-alloyed AlSi10Mg powder. Acta Mater 2013;61:1809–19. https://doi.org/10.1016/j.actamat.2012.11.052.

[42] Wu J, Wang XQ, Wang W, Attallah MM, Loretto MH. Microstructure and strength of selectively laser melted AlSi10Mg. Acta Mater 2016;117:311–20. https://doi.org/10.1016/j.actamat.2016.07.012.

[43] Guan Y, Chen B, Zou J, Britton TB, Jiang J, Dunne FPE. Crystal plasticity modelling and HR-DIC measurement of slip activation and strain localization in single and oligo-crystal Ni alloys under fatigue. Int J Plast 2017;88:70–88. https://doi.org/10.1016/j.ijplas.2016.10.001.

[44] Bachmann F, Hielscher R, Schaeben H. Grain detection from 2d and 3d EBSD data—Specification of the MTEX algorithm. Ultramicroscopy 2011;111:1720–33. https://doi.org/10.1016/j.ultramic.2011.08.002.

[45] Romanova V, Balokhonov R, Zinovieva O, Emelianova E, Dymnich E, Pisarev M, et al. Micromechanical simulations of additively manufactured aluminum alloys. Comput Struct 2021;244. https://doi.org/10.1016/j.compstruc.2020.106412.

[46] Paul MJ, Liu Q, Best JP, Li X, Kruzic JJ, Ramamurty U, et al. Fracture resistance of AlSi10Mg fabricated by laser powder bed fusion. Acta Mater 2021;211. https://doi.org/10.1016/j.actamat.2021.116869.

[47] Aboulkhair NT, Maskery I, Tuck C, Ashcroft I, Everitt NM. Improving the fatigue behaviour of a selectively laser melted aluminium alloy: Influence of heat treatment and surface quality. Mater Des 2016;104:174–82. https://doi.org/10.1016/j.matdes.2016.05.041.

[48] Littlewood PD, Wilkinson AJ. Geometrically necessary dislocation density distributions in cyclically deformed Ti–6Al–4V. Acta Mater 2012;60:5516–25. https://doi.org/10.1016/j.actamat.2012.07.003.

[49] Anand L, Kalidindi SR. The process of shear band formation in plane strain compression of fcc metals: Effects of crystallographic texture. Mech Mater 1994;17: 223–43. https://doi.org/10.1016/0167-6636(94)90062-0.

[50] Littlewood PD, Wilkinson AJ. Local deformation patterns in Ti–6Al–4V under tensile, fatigue and dwell fatigue loading. Int J Fatigue 2012;43:111–9. https://doi.org/10.1016/j.ijfatigue.2012.03.001.

[51] Zhao C, Stewart D, Jiang J, Dunne FPE. A comparative assessment of iron and cobalt-based hard-facing alloy deformation using HR-EBSD and HR-DIC. Acta Mater 2018;159:173–86. https://doi.org/10.1016/j.actamat.2018.08.021.

[52] Tillmann W, Schaak C, Nellesen J, Schaper M, Aydinöz ME, Hoyer KP. Hot isostatic pressing of IN718 components manufactured by selective laser melting. Addit Manuf 2017;13:93–102. https://doi.org/10.1016/j.addma.2016.11.006.

[53] Molaei R, Fatemi A, Phan N. Significance of hot isostatic pressing (HIP) on multiaxial deformation and fatigue behaviors of additive manufactured Ti-6Al-4V

including build orientation and surface roughness effects. Int J Fatigue 2018;117:352–70. https://doi.org/10.1016/j.ijfatigue.2018.07.035.

[54] Yu H, Li F, Wang Z, Zeng X. Fatigue performances of selective laser melted Ti-6Al-4V alloy: Influence of surface finishing, hot isostatic pressing and heat treatments. Int J Fatigue 2019;120:175–83. https://doi.org/10.1016/j.ijfatigue.2018.11.019.

[55] Arnaudov N, Kolyshkin A, Weihe S. Micromechanical modeling of fatigue crack initiation in hydrogen atmosphere. Mech Mater 2020;149:103557. https://doi.org/10.1016/j.mechmat.2020.103557.